

# Construction of Built-In Electric Field within Silver Phosphate Photocatalyst for Enhanced Removal of Recalcitrant Organic Pollutants

Yan Lin, Chunping Yang,\* Shaohua Wu,\* Xiang Li, Yingjie Chen, and William L. Yang

Semiconductor photocatalysis technology has aroused great interest in photocatalytic degradation, but it suffers from the drawbacks of fast electron-hole recombination and unsatisfactory degradation efficiency. Herein, a novel photocatalyst  $\text{Ag}_3\text{PO}_4@\text{NC}$  with excellent photocatalytic activity is successfully prepared, characterized, and evaluated for the efficient removal of organic pollutants. After visible light irradiation for 5, 8, and 12 min, the photocatalytic degradation efficiency of norfloxacin, diclofenac, and phenol on the composite catalyst reaches 100%, and the apparent rate constant of which is 19.2, 48.7, and 23.2 times than that of the pure  $\text{Ag}_3\text{PO}_4$ , respectively. The density functional theory calculation results indicate that there is a built-in electric field from N-doped carbon (NC) to  $\text{Ag}_3\text{PO}_4$  at the interface of the composite catalyst. Driven by the electric field, the photogenerated electrons of  $\text{Ag}_3\text{PO}_4$  can be readily transferred to the NC, leading to the efficient separation of photogenerated carriers and the significant improvement of the catalytic performance. The results of radical trapping experiments and electron spin resonance analysis show that photogenerated holes and  $\text{O}_2^-$  play an important role in the photodegradation process. This work provides a universal strategy of construction built-in electric field through coupling with NC to improve the photocatalytic performance of photocatalysts.

one of the most serious problems nowadays. For example, the annual output of phenol in China is about 6 million tons,<sup>[1]</sup> and the phenol-contaminated wastewater has become a typical high-toxicity industrial wastewater.<sup>[2]</sup> Moreover, pharmaceuticals and personal care products (PPCPs), as emerging organic toxicants, also have garnered increasing attention globally.<sup>[3,4]</sup> For instance, the pharmaceutical diclofenac is one of the most popular non-steroidal anti-inflammatory drugs with a global annual consumption of up to 1000 tons, and it is frequently detected in the treated wastewater, rivers, lakes, and even drinking water.<sup>[5,6]</sup> Norfloxacin is a kind of fluoroquinolone antibiotics used in the treatment of bacterial infections, aquaculture industry, and livestock, which is often detected in wastewater effluents.<sup>[7]</sup> Because these chemical productions are toxic and refractory to traditional biological treatment, it is urgent to develop efficient and environment-friendly treatment technology.

## 1. Introduction


With the rapid development of industry, the increasingly severe environmental pollution and ecological destruction has become

Solar photocatalysis based on semiconductor materials is considered to be a promising technology, which can utilize solar energy to decompose organic contaminants.<sup>[8,9]</sup> However, due to the high recombination rate of charge carrier and low utilization efficiency of light energy, the photoenergy conversion efficiency of catalyst is still unsatisfactory, which seriously limits its practical application.<sup>[10]</sup> The key to break through this bottleneck is to design and develop new catalysts with good visible light response and high photocatalytic activity. As an excellent photocatalyst,  $\text{Ag}_3\text{PO}_4$  has attracted intense interest due to its advantages of high quantum efficiency (>90%), superior oxidative ability, and simple preparation process.<sup>[11,12]</sup> Despite the fact that  $\text{Ag}_3\text{PO}_4$  possess superior properties, the disadvantages of readily formation irregular microstructure in the preparation process and photocorrosion in the photocatalytic process severely hamper its wide applications.<sup>[13]</sup> In order to overcome these weaknesses and improve its photocatalytic performance, numerous methods were adopted.<sup>[14,15]</sup> The efforts mainly included controlling the crystal morphology,<sup>[16]</sup> facet engineering,<sup>[17]</sup> metal deposition,<sup>[18]</sup> ion doping,<sup>[19]</sup> or coupling with another semiconductor.<sup>[20]</sup> All these attempts demonstrate that the key to solve the problem is to achieve effective spatial separation and rapid transfer of photogenerated charges to the surface reaction sites.

Y. Lin, Prof. C. P. Yang, Dr. S. H. Wu, X. Li, Y. J. Chen, W. L. Yang  
College of Environmental Science and Engineering  
Hunan University  
and Key Laboratory of Environmental Biology and Pollution Control  
(Hunan University)  
Ministry of Education  
Changsha, Hunan 410082, China  
E-mail: yangc@hnu.edu.cn; wushaohua@hnu.edu.cn

Y. Lin, Prof. C. P. Yang, Dr. S. H. Wu, X. Li  
Guangdong Provincial Key Laboratory of Petrochemical Pollution  
Processes and Control  
School of Environmental Science and Engineering  
Guangdong University of Petrochemical Technology  
Maoming, Guangdong 525000, China

Prof. C. P. Yang  
Hunan Provincial Environmental Protection Engineering Center for  
Organic Pollution Control of Urban Water and Wastewater  
Changsha, Hunan 410001, China

 The ORCID identification number(s) for the author(s) of this article can be found under <https://doi.org/10.1002/adfm.202002918>.

DOI: 10.1002/adfm.202002918

Construction of built-in electric field at interface of catalysts is considered as an effective approach to achieve maximum carrier separation, because it can be used as the driving force for charge separation that drives the targeted surface reaction in the photocatalytic systems.<sup>[21]</sup> Specifically, the photogenerated electrons will reverse transfer under the driving of electric field, thus drastically expedites the separation of electron-hole pairs. For example, Yu et al. established the built-in electric field through gradual doping of graphited carbon rings within g-C<sub>3</sub>N<sub>4</sub>, achieving a 21-fold improvement in the photocatalytic hydrogen evolution rate.<sup>[22]</sup> Cui et al. proposed the p-n homojunction perovskite solar cells whose built-in electric field promotes oriented transport of the photoinduced carriers, thus reducing carrier recombination losses and enhancing power conversion efficiency.<sup>[23]</sup> These successful cases illustrated that constructing built-in electric field is a promising route to suppress the recombination of carriers and further improve the performances of photocatalysts.

In the case of Ag<sub>3</sub>PO<sub>4</sub> photocatalytic system, in addition to the built-in electric field, a good electron acceptor is needed to accommodate photogenerated electrons rapidly to inhibit its photocorrosion. Due to the advantages of good electric conductivity, low cost, tunable structural and optoelectronic properties, carbonaceous materials are always chosen as functional additives to ameliorate the performance of materials.<sup>[24,25]</sup> For instance, the photocatalytic activity of TiO<sub>2</sub> was significantly improved through the surface hybridization of TiO<sub>2</sub> with graphite-like carbon layers, which was due to the mediating role of carbon layer in storing and shuttling photogenerated electrons from the catalysts to the acceptor in the photocatalytic process.<sup>[25]</sup> In addition, nitrogen doping is regarded as a promising method to further increase the electronic conductivity of carbon-based materials and enhance its chemical performances.<sup>[26,27]</sup> For example, Liu et al. reported that nitrogen-doped carbon materials showed outstanding electrocatalytic activity, long-term stability, and excellent resistance to crossover effects for oxygen-reduction reaction.<sup>[27]</sup> On the other hand, it is believed that the hollow architectures can not only shorten the distance of charge transport to expedite the separation of photogenerated charges, but also afford large surface area and abundant active sites to promote redox reactions.<sup>[28,29]</sup>

Therefore, it can be deduced that the hollow N-doped carbon (NC) material is a promising candidate for the construction of built-in electric field to promote carrier oriented migration and serve as the receptor of photogenerated electrons. Combined with the advantages of above strategies for the design of Ag<sub>3</sub>PO<sub>4</sub>-based catalysts, it is expected to improve the charge separation efficiency of Ag<sub>3</sub>PO<sub>4</sub>, inhibit its photocorrosion, and improve its photocatalytic activity. More importantly, this universal design strategy has the potential to inspire the development of highly efficient photocatalysts, yet it is still to report.

In this study, N-doped carbon with hollow structure was prepared as the photogenerated electron trap centers, and the built-in electric field at interface was constructed to induce the oriented transport of photogenerated carriers. Specifically, the novel photocatalyst Ag<sub>3</sub>PO<sub>4</sub>@NC was synthesized for the first time, and its carrier separation efficiency, photostability, catalytic activity, and catalytic mechanism were fully investigated. The results indicated that after the coupling with NC, the

charge separation efficiency and photostability of Ag<sub>3</sub>PO<sub>4</sub> was significantly improved. The Ag<sub>3</sub>PO<sub>4</sub>@NC composite achieved excellent photocatalytic degradation efficiency of norfloxacin, diclofenac, and phenol, and the corresponding apparent rate constant was 1.248, 0.925, and 0.721 min<sup>-1</sup>, respectively, which was 19.2, 48.7, and 23.2 times than that of the pure Ag<sub>3</sub>PO<sub>4</sub>, respectively. Experimental evidences and DFT calculations demonstrated that there was a built-in electric field at interface, which facilitated the rapid transfer of photogenerated charge and consequently led to the excellent photocatalytic activity for pollutants degradation.

## 2. Results and Discussion

### 2.1. Characterization of Materials

The preparation process of the NC with hollow structure is depicted in Figure S1, Supporting Information. The MnO<sub>2</sub> nanowires with high aspect ratio were first synthesized as the starting template. Then, the MnO<sub>2</sub>@PDA composite was obtained after the addition of dopamine hydrochloride, and the SEM images of MnO<sub>2</sub>@PDA are shown in **Figure 1a**. It could be observed that the surface of MnO<sub>2</sub> was perfectly coated by PDA, and the 1D linear structure was well preserved. Subsequently, the MnO<sub>2</sub>@PDA composite was carbonized in the N<sub>2</sub> atmosphere to yield the core-shell MnO<sub>2</sub>@NC nanotube. The FESEM image in Figure 1b revealed that the MnO<sub>2</sub>@NC with slightly rougher surface was formed after annealing. Moreover, the TEM images also indicted the formation of perfect core-shell MnO<sub>2</sub>@NC nanotubes with an ultrathin NC shell of about 6 nm (Figure 1e,f). HRTEM image showed the clear lattice fringes with an interplanar spacing of 0.241 nm (Figure 1f), which corresponded to the (211) plane of MnO<sub>2</sub> (JCPDS no. 44-0141). Afterward, the MnO<sub>2</sub>@NC composite was treated with acid to remove the MnO<sub>2</sub> templates, and the hollow NC nanotubes were obtained (Figure 1c).

Finally, the Ag<sub>3</sub>PO<sub>4</sub>@NC was prepared using an electrostatic driven self-assembly method. As shown in Figure S2a,b, Supporting Information, compared with the pure Ag<sub>3</sub>PO<sub>4</sub>, after the introduction of NC, larger Ag<sub>3</sub>PO<sub>4</sub> particles with a diameter of about 10–20 μm all turned into much smaller crystal particles. The phenomena could be ascribed to the electrostatic driving assembly between the negatively charged NC and the positively charged Ag<sup>+</sup>.<sup>[30]</sup> As presented in Figure 1d,g, it could be seen clearly that the NC nanotubes have good contact with the Ag<sub>3</sub>PO<sub>4</sub> crystal, and some Ag<sub>3</sub>PO<sub>4</sub> particles were grown along the surface of NC. The interplanar spacing of 0.245 nm could be clearly observed in the HRTEM image of Figure 1h, which corresponded to the (211) crystal planes of Ag<sub>3</sub>PO<sub>4</sub> (JCPDS No.06-0505). Besides, the elemental mapping images of Ag<sub>3</sub>PO<sub>4</sub>@NC composite were provided in Figure S4, Supporting Information, indicating that the NC nanotubes were evenly distributed in the Ag<sub>3</sub>PO<sub>4</sub>@NC composite. The above results suggested that the NC nanotubes were successfully introduced into the Ag<sub>3</sub>PO<sub>4</sub>@NC composite, and good interface contact between them was also established.

The XRD patterns of as-prepared samples are provided in **Figure 2a**. For the pure Ag<sub>3</sub>PO<sub>4</sub> and Ag<sub>3</sub>PO<sub>4</sub>@NC composite,



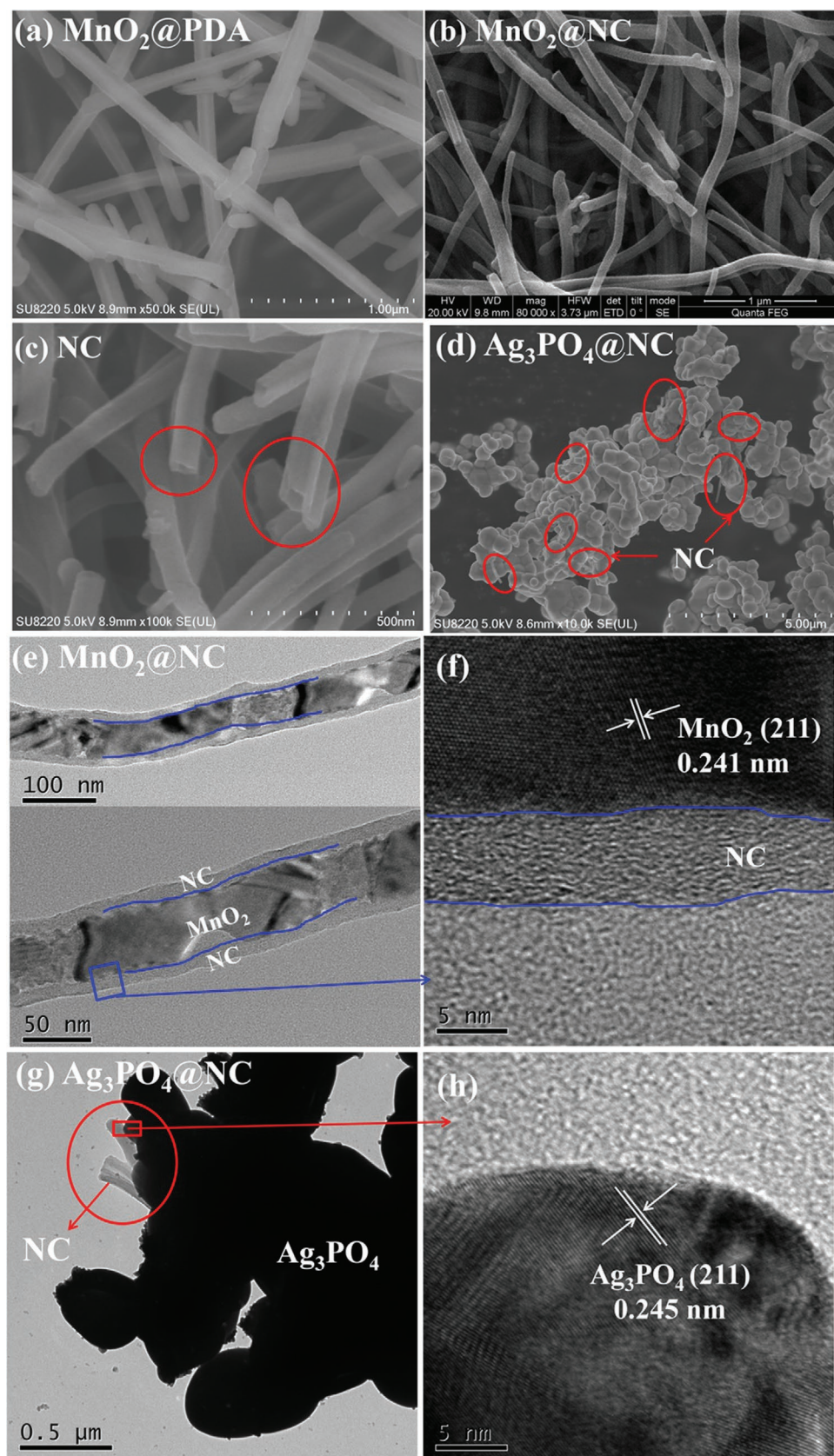


**Figure 1.** SEM images of  $\text{MnO}_2@\text{PDA}$  a),  $\text{MnO}_2@\text{NC}$  b), NC c), and  $\text{Ag}_3\text{PO}_4@\text{NC}$  d); HRTEM image of  $\text{MnO}_2@\text{NC}$  e,f) and  $\text{Ag}_3\text{PO}_4@\text{NC}$  g,h).

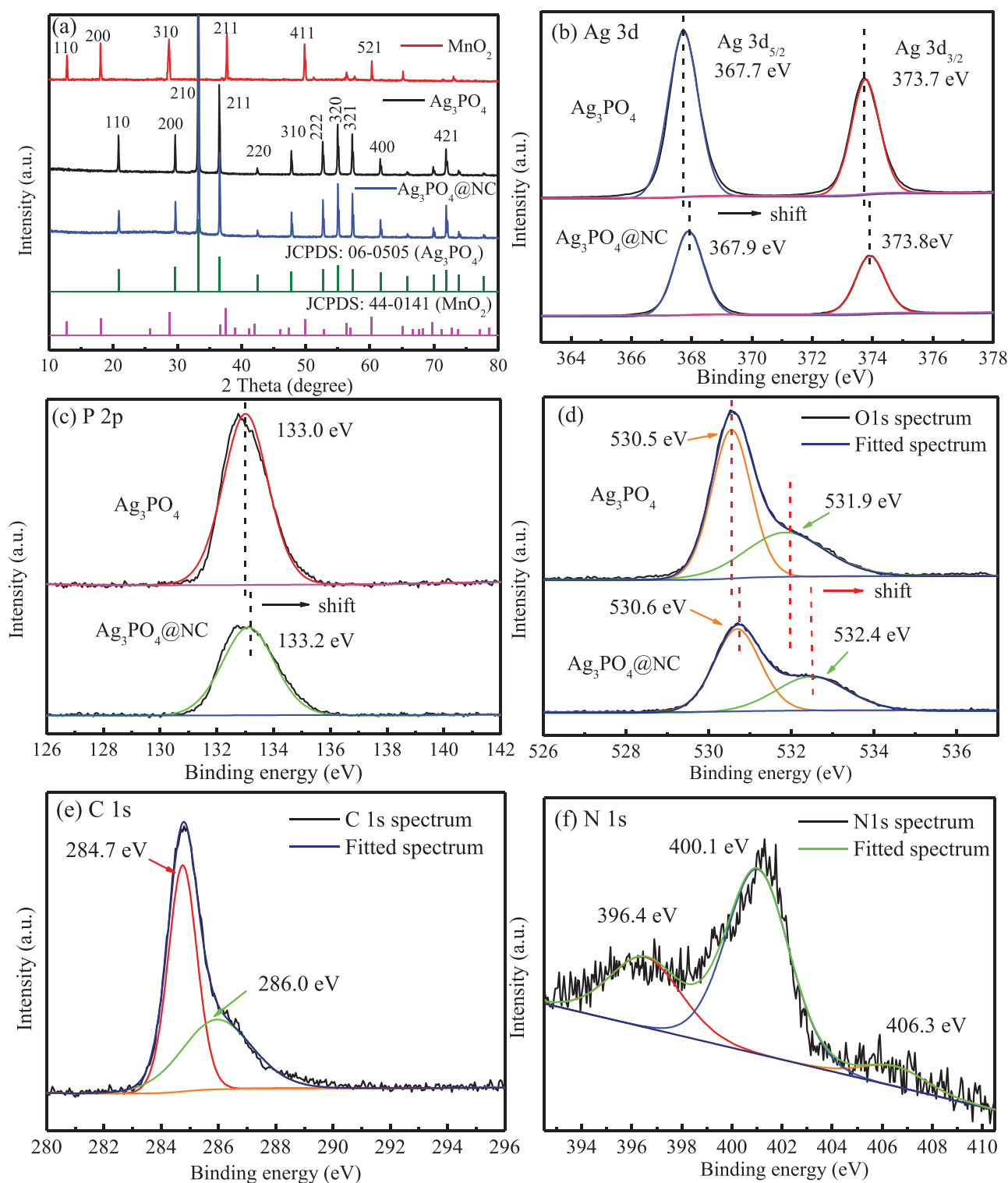


**Figure 2.** XRD pattern of different samples a), high resolution XPS spectrum of b) Ag 3d, c) P 2p, d) O 1s, e) C 1s, and f) N 1s of  $\text{Ag}_3\text{PO}_4@NC$ .

all the diffraction peaks can be indexed to the typical body-centered cubic structure (JCPDS No. 06-0505). Interestingly, although the position of the diffraction peaks was almost the same after the introduction of NC, the intensity of the diffraction peaks varied significantly in different crystal planes.

For the  $\text{Ag}_3\text{PO}_4@NC$  composite, the intensity ratio of (222) and (110) diffraction peaks was 1.35, which was significantly higher than that of the pure  $\text{Ag}_3\text{PO}_4$  (0.847), indicating that more (222) crystalline planes of  $\text{Ag}_3\text{PO}_4$  was exposed after the coupling of NC. According to the previous studies, the {111}

plane possesses the highest surface energy ( $1.65 \text{ J m}^{-2}$ ), over two times higher than the  $\{110\}$  surfaces ( $0.78 \text{ J m}^{-2}$ ).<sup>[17]</sup> Moreover, higher surface energy of facets contributed to improve the photocatalytic activity of catalyst.<sup>[14]</sup> Therefore, the introduction of NC could contribute to the better crystal facets exposure of  $\text{Ag}_3\text{PO}_4$ , leading to high active surface reaction sites and excellent photocatalytic performance.

The XPS spectra of different samples are provided in Figure 2b–f. In case of the pure  $\text{Ag}_3\text{PO}_4$ , two peaks positioned at binding energy of 367.7 and 373.7 eV in Ag 3d spectrum could be assigned to the electron orbits of Ag  $3d_{5/2}$  and Ag  $3d_{3/2}$  of  $\text{Ag}^+$ , respectively (Figure 2b). The peak with binding energy at 133.0 eV could be ascribed to the P 2p of  $\text{PO}_4^{3-}$  (Figure 2c). The O 1s spectrum was divided into two different peaks, 530.5 and 531.9 eV, which corresponded to the lattice oxygen and surface oxygen of  $\text{Ag}_3\text{PO}_4$ , respectively. As for the  $\text{Ag}_3\text{PO}_4/\text{NC}$  composite, the XPS spectra in Figure S5, Supporting Information, indicated that all signals of Ag, P, O, C, and N were clearly observed. The spectrum of C 1s could be divided into two peaks (Figure 2e). The main peak at 284.7 eV corresponded to the graphite-like  $\text{sp}^2$  C, and the small peak at 286.0 eV was attributed to the N- $\text{sp}^2$  C bonds.<sup>[31,32]</sup> The N 1s spectrum was deconvoluted into three peaks located at 396.4, 400.1, and 406.3 eV, which were assigned to the C–N, C = N, and N–O bonds, respectively (Figure 2f).<sup>[33,34]</sup> It was worth noting that after the introduction of NC, the signal peaks of Ag, C, and O all shifted to the positive position, implying the strong interface interaction between  $\text{Ag}_3\text{PO}_4$  and NC.

The optical properties of the samples were investigated by UV–vis absorption spectroscopy, and the results are shown in Figure 3a. Obviously, the optical absorption of the composite photocatalyst was significantly enhanced after the introduction of NC. The drastically strengthened optical adsorption of composite catalyst indicated that  $\text{Ag}_3\text{PO}_4$  and NC were successfully coupled, and the  $\text{Ag}_3\text{PO}_4/\text{NC}$  composite could use visible light efficiently and acquire more photogenerated electron–hole pairs. In addition, the band gap energy of  $\text{Ag}_3\text{PO}_4$  calculated by the Kubelka–Munk equation was 2.34 eV (Figure S6a, Supporting Information). The Mott–Schottky (MS) plots of  $\text{Ag}_3\text{PO}_4$  and  $\text{Ag}_3\text{PO}_4/\text{NC}$  were also measured and presented in Figure 3b, which indicated that as-prepared samples were typical n-type semiconductors with overall positive slopes. The applied potential of  $\text{Ag}_3\text{PO}_4$  was 0.43 V versus SCE, so the flat band potential was determined as 0.40 V, which was equal to 0.64 V versus NHE. The conduction band and valence band potential of  $\text{Ag}_3\text{PO}_4$  was calculated as 0.44 and 2.78 V versus NHE, respectively, and details are provided in the Supporting Information. In order to further confirm the band potential, the XPS valence band analysis was performed and the results are shown in Figure S6b,c, Supporting Information. The valence band potential of  $\text{Ag}_3\text{PO}_4$  was measured to be 2.78 eV, which was consistent with the results of MS plots. Moreover, the flat band potential of  $\text{Ag}_3\text{PO}_4/\text{NC}$  composite showed a slight negative shift of 0.07 V compared with that of pure  $\text{Ag}_3\text{PO}_4$ , implying the electronic interactions between  $\text{Ag}_3\text{PO}_4$  and NC.<sup>[35]</sup>

To investigate the photogenerated charge separation of as-prepared photocatalysts, the photoluminescence (PL) spectra measurement was conducted. As displayed in Figure 3c,

compared with the pure  $\text{Ag}_3\text{PO}_4$ , the  $\text{Ag}_3\text{PO}_4/\text{NC}$  composite presented much lower fluorescence signal peak intensity, indicating that the recombination rate of photogenerated electron–hole pairs was effectively inhibited after the introduction of NC. In addition, the carrier lifetime of the samples was studied by TRPL decay spectra, and the obtained data were fitted by biexponential decay function (Figure 3d). The detailed analysis can be found in the Supporting Information, and the fitting parameters are listed in Table S1, Supporting Information. It could be found that the  $\text{Ag}_3\text{PO}_4$  have two lifetimes, 2.79 and 24.48 ns, respectively. The short decay time component is considered to be due to the quasi-free excitons, while the long component is attributed to the localized exciton recombination, which is caused by de-trapping of carriers.<sup>[36,37]</sup> The results indicated that the lifetime of  $\text{Ag}_3\text{PO}_4/\text{NC}$  composite (5.18 ns) was much shorter than that of  $\text{Ag}_3\text{PO}_4$  (11.72 ns), suggesting an additional nonradiative decay channel was opened and the effective charge was transferred from  $\text{Ag}_3\text{PO}_4$  to NC.<sup>[36]</sup>

Moreover, the photocurrent responses of the samples were also tested. It could be observed that the transient photocurrent responses of the samples exhibited repeatable and relatively stable photocurrent profiles during the successive light on and off cycles (Figure 3e). Obviously, under the identical condition, the  $\text{Ag}_3\text{PO}_4/\text{NC}$  composite presented much higher photocurrent density than that of the pure  $\text{Ag}_3\text{PO}_4$ , which further demonstrated that an effective interfacial charge separation process was achieved through the combination of  $\text{Ag}_3\text{PO}_4$  and NC. Besides, the change of electrochemical impedance spectroscopy (EIS) is related to the interfacial properties of materials. The presence of the built-in electric field can promote the migration and separation of the photogenerated charge at the interface, and the reduction of the impedance is one of the intuitive manifestations of this phenomenon.<sup>[38]</sup> As shown in Figure 3f, the arc radius of EIS Nyquist plots of  $\text{Ag}_3\text{PO}_4/\text{NC}$  composite was much smaller than that of pure  $\text{Ag}_3\text{PO}_4$ , indicating that the electron transfer ability of the composite catalyst was much better than that of the  $\text{Ag}_3\text{PO}_4$ . Based on the above analysis, it could be deduced that the introduction of NC significantly improved the efficiency of charge separation and produced more effective charges in the photocatalytic reaction system of composite catalyst.

## 2.2. Photocatalytic Degradation of Organic Pollutants, Photostability of Photocatalysts, and Active Species in Photocatalytic Reaction

The photocatalytic activity of as-prepared samples was evaluated for the degradation of phenol, DFC, and NFL. As shown in Figure 4a, the pure  $\text{Ag}_3\text{PO}_4$  exhibited unsatisfactory catalytic activity, and the removal efficiency of phenol was only 29.5% after 12 min of visible light irradiation. Obviously, compared with pure  $\text{Ag}_3\text{PO}_4$ , all binary photocatalysts showed much better photocatalytic performance, and the  $\text{Ag}_3\text{PO}_4/\text{NC}$  composite possessed the highest catalytic activity. In addition, the degradation experimental data were simulated by the pseudo-first-order kinetic model,<sup>[39–41]</sup> and the results are shown in Figure S7, Supporting Information. The rate constant (*k*) of phenol degradation by  $\text{Ag}_3\text{PO}_4/\text{NC}$  composite was



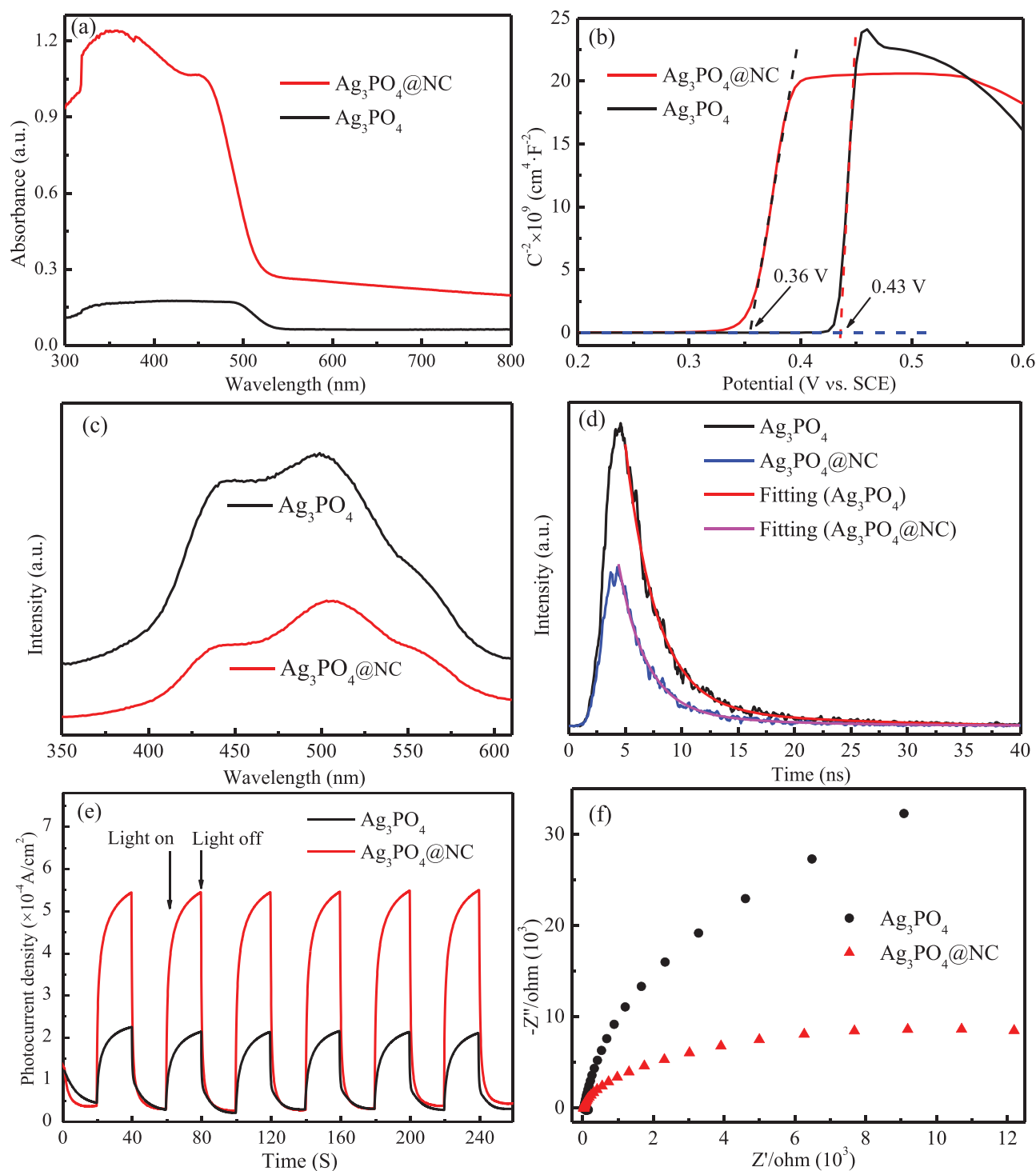


**Figure 3.** a) UV-vis absorption spectra, b) Mott-Schottky plots, c) PL spectra, d) TRPL decay spectra, e) photocurrent response density, and f) EIS Nyquist plots of as-prepared samples.

$0.721 \text{ min}^{-1}$ , which was about 23 times than that of pure  $\text{Ag}_3\text{PO}_4$  ( $0.031 \text{ min}^{-1}$ ). Similarly, for the degradation of DFC and NFL, the  $\text{Ag}_3\text{PO}_4@75 \text{ mL NC}$  composite still exhibited the best photocatalytic performance, and the 100% removal of these two kinds of pollutants only took 8 and 5 min, respectively (Figure 4b,c). As shown in Figure S7b,c, Supporting Information, the

apparent rate constants of  $\text{Ag}_3\text{PO}_4@75 \text{ mL NC}$  composite on the degradation of DFC and NFL were 48.7 and 19.2 times higher than that of the pure  $\text{Ag}_3\text{PO}_4$ , respectively. Moreover, in order to further evaluate the photocatalytic activity of as-prepared catalyst, the photocatalytic performance of  $\text{Ag}_3\text{PO}_4@NC$  was compared with other reported Ag-based photocatalysts and

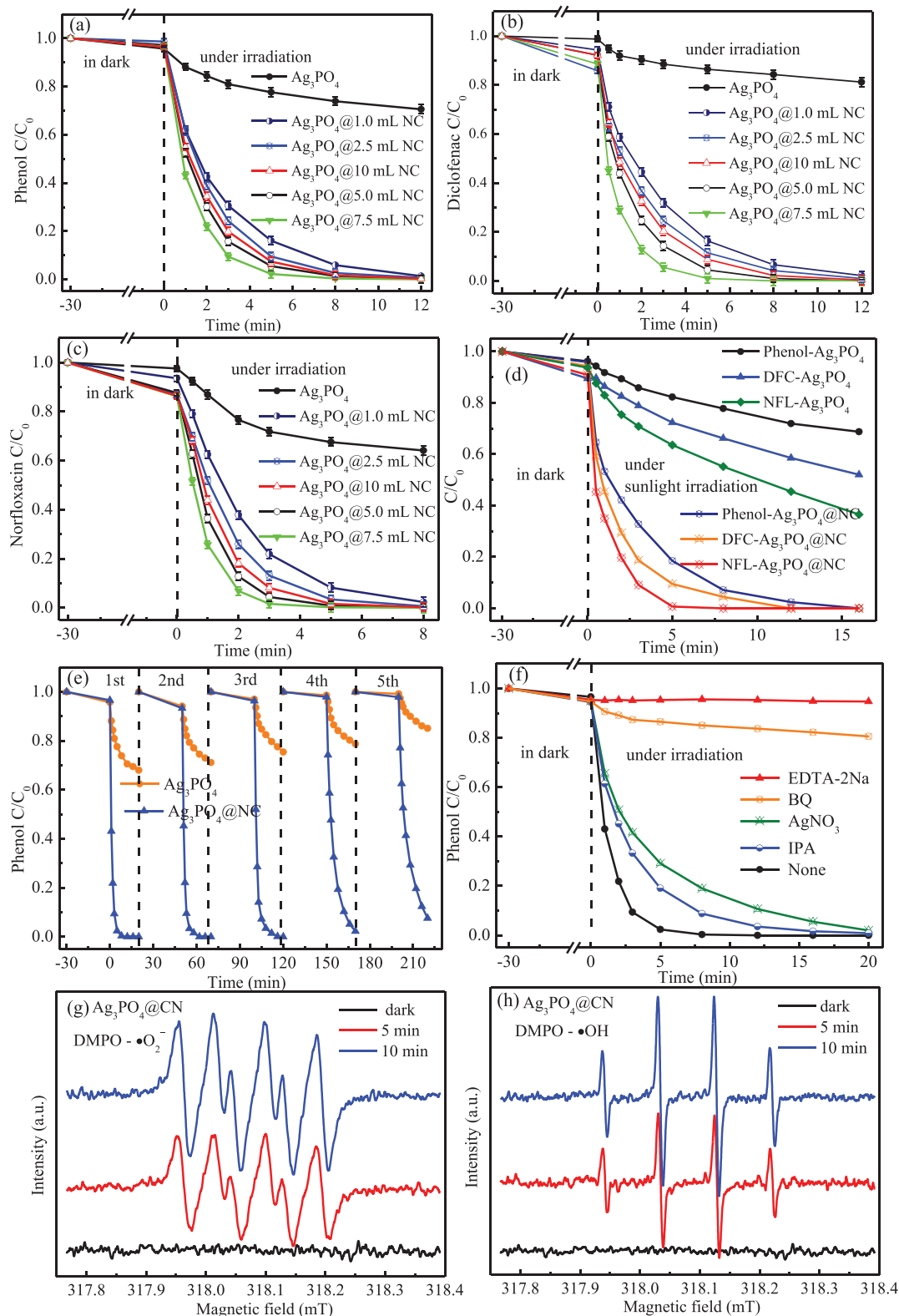


**Figure 4.** Photodegradation curves of phenol a), DFC b), and NFL c) in the presence of as-prepared samples; d) photodegradation curves of different pollutants under the natural sunlight irradiation with different samples; e) cycling test for the photocatalytic degradation of phenol in the presence of different samples; f) photodegradation curves of phenol over  $Ag_3PO_4@NC$  composite with different active species scavengers; ESR spectra of radical adducts trapped by DMPO in the different samples dispersion under both the dark and visible light irradiation ( $\lambda > 420$  nm) condition: g) in methanol dispersion for  $DMPO - O_2^-$ ; h) in aqueous dispersion for  $DMPO - OH$ .

materials. The comparison results are provided in Tables S4 and S5, respectively. Comprehensive consideration and comparison the apparent rate constant, removal rate and reaction time, it could be found that the photocatalytic performance of  $\text{Ag}_3\text{PO}_4@\text{NC}$  prepared in this study was obviously better than that of previous reported Ag-based photocatalysts and other materials. The above results suggested that the photocatalytic activity of  $\text{Ag}_3\text{PO}_4$  was dramatically improved after the introduction of NC, which may result from the efficient separation of photogenerated carriers at the interface of  $\text{Ag}_3\text{PO}_4$  and NC.

In consideration of the practical application value of as-prepared photocatalysts, the degradation performance of different pollutants under natural sunlight irradiation was carried out.<sup>[42,43]</sup> The corresponding solar intensity and the HPLC chromatogram of phenol, DFC, and NFL degradation over  $\text{Ag}_3\text{PO}_4@\text{NC}$  composite are provided in Table S2 and Figure S8, Supporting Information, respectively. As presented in Figure S8, Supporting Information, and Figure 4d, the retention time of the characteristic peaks for phenol, DFC, and NFL was 4.47, 4.57, and 3.96 min, respectively, and the characteristic peaks of which gradually weaken with the increased irradiation time and disappeared completely after 16, 12, and 5 min, respectively. The results indicated that the  $\text{Ag}_3\text{PO}_4@\text{NC}$  composite still showed excellent photocatalytic activity under sunlight irradiation, that is, as-prepared photocatalysts could effectively utilize natural sunlight for environmental treatment.

The photostability and reusability of photocatalyst are another important factors affecting its practical application. As shown in Figure 4e, with the increase of recycling times, the photocatalytic activity of  $\text{Ag}_3\text{PO}_4$  decreased obviously, and the removal efficiency of phenol decreased from 32% to 15%. The XRD results in Figure S9, Supporting Information, indicated that compared with the fresh  $\text{Ag}_3\text{PO}_4$ , two distinct peaks located at  $38.12^\circ$  and  $44.28^\circ$  appeared on the pattern of recycled  $\text{Ag}_3\text{PO}_4$ , which corresponded to the (111) and (200) plane of metallic Ag, respectively. The significant loss of photocatalytic performance was mainly attributed to its serious photocorrosion, which made the  $\text{Ag}^+$  in  $\text{Ag}_3\text{PO}_4$  crystal be reduced to metallic Ag, thus the  $\text{Ag}_3\text{PO}_4$  crystal structure was destroyed and the light absorption performance was also declined due to its surface covered with metallic Ag.<sup>[44,45]</sup> However, the  $\text{Ag}_3\text{PO}_4@\text{NC}$  composite still showed good reusability after being recycled and repeatedly used five times. After three consecutive cycles, the degradation efficiency of phenol was still at 100%. After the fourth and fifth cycles, the degradation rates also went up to 97% and 92%, respectively. The XRD pattern of the recycled  $\text{Ag}_3\text{PO}_4@\text{NC}$  composite has no obvious change compared with the original one, only a weak diffraction peak at  $38.12^\circ$  was observed, indicating that the  $\text{Ag}_3\text{PO}_4@\text{NC}$  composite possess good anti-photocorrosion ability. In view of the  $\text{Ag}_3\text{PO}_4@\text{NC}$  composite has the excellent performance in natural sunlight condition and its good photostability, it could be considered as a promising and effective photocatalyst in environmental remediation.

In order to explore the predominant active species generated in the degradation process, the trapping experiment was carried out by adding different scavengers of active species.<sup>[46,47]</sup> As shown in Figure 4f, almost complete deactivation of the photocatalyst was observed in the presence of EDTA-2Na, suggesting

the active species of holes played an important role in the photocatalytic degradation process. This phenomenon also demonstrated that the highly positive valence band position of  $\text{Ag}_3\text{PO}_4$  makes its photogenerated holes possess strong oxidation ability. The photocatalytic activity of catalysts was severely inhibited after the addition of BQ, indicating that the  $\cdot\text{O}_2^-$  was another main active specie involved in photocatalytic degradation. In the presence of  $\text{AgNO}_3$ , the photocatalytic activity also decreased, suggesting that the photogenerated electrons also participated in the degradation reaction. As for IPA, compared with the above scavengers, its inhibition on the activity of catalyst was relatively low, but the contribution of  $\cdot\text{OH}$  to the pollutant removal rate should not be ignored. It can be concluded that  $\cdot\text{O}_2^-$ ,  $\cdot\text{OH}$ , photogenerated holes, and electrons all worked in the photocatalytic degradation process, among which the photogenerated holes and  $\cdot\text{O}_2^-$  played the most important role. Moreover, to further verify the generation of active oxygen species in the photocatalytic process, the electron spin resonance (ESR) spin-trap technology was also performed, and the experiments were operated under dark condition and visible light irradiation of 5 and 10 min. No signal peak appeared in the dark, whereas the strong characteristic peak of  $\text{DMPO}\cdot\text{O}_2^-$  was observed after the visible light irradiation, and the peak intensity became stronger with the extension of the light time, demonstrating that  $\cdot\text{O}_2^-$  played a crucial role in the photocatalytic process (Figure 4g). As presented in Figure 4h, the ESR signal splits into two sets of four strong single lines with an intensity ratio of 1:2:2:1, unambiguously indicating  $\cdot\text{OH}$  generation in the photocatalytic process.<sup>[48,49]</sup>

### 2.3. Photocatalytic Mechanisms on the Basis of DFT Calculations

DFT calculations were performed to reveal the photo-generated charge migration mechanism in  $\text{Ag}_3\text{PO}_4@\text{NC}$  composite. In order to evaluate the accuracy of the computing method used to calculate the properties of electronic structures, the band structure of bulk  $\text{Ag}_3\text{PO}_4$  was first calculated with different approaches. As shown in Figure S11, Supporting Information, the computational indirect band gap from GGA-PBE was 0.12 eV, which significantly underestimated the experimental results (2.34 eV). Therefore, more suitable calculation method is needed, and the electronic structure calculations based on the density-functional theory DFT+U approach were thus conducted, by which the band gap of bulk  $\text{Ag}_3\text{PO}_4$  was calculated as 2.26 eV (Figure 5a). The profile of the planar averaged electrostatic potential for  $\text{Ag}_3\text{PO}_4$  and  $\text{Ag}_3\text{PO}_4@\text{NC}$  composite as a function of position in the  $z$ -direction was displayed in Figure S10c, Supporting Information, and Figure 5b, respectively. The periodic lattice potential in the  $\text{Ag}_3\text{PO}_4(100)$  could be clearly observed in Figure S10c, Supporting Information, but there was a big built-in potential well appeared at interfaces between the  $\text{Ag}_3\text{PO}_4(100)$  and NC in the composite, implying the interfacial charge transfer.

The 3D charge density difference was calculated to investigate the charge transfer and redistribution at the interface of  $\text{Ag}_3\text{PO}_4(100)$  and NC, and the results are depicted in Figure 5c.



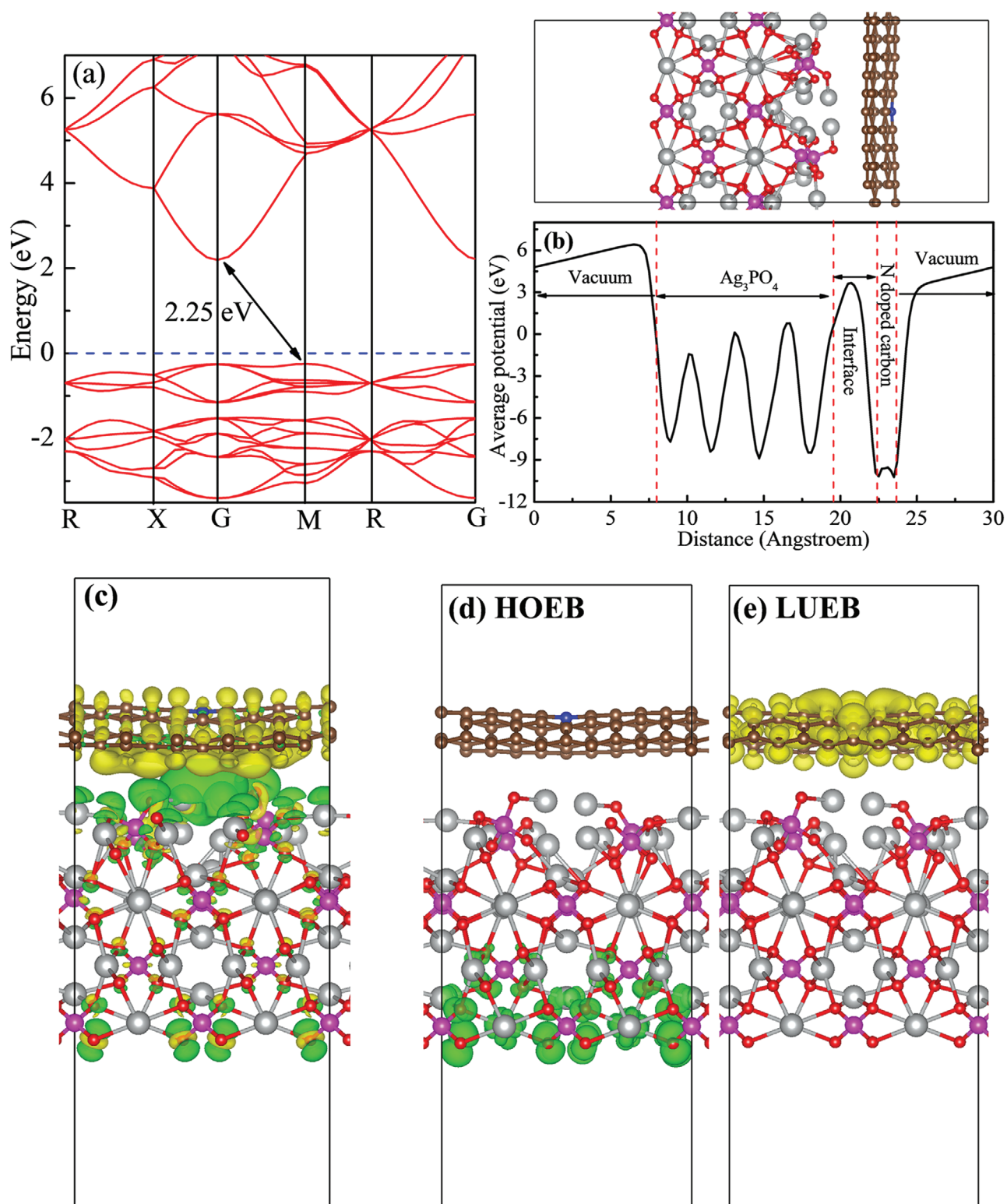


**Figure 5.** a) The band structure of bulk  $\text{Ag}_3\text{PO}_4$  using standard DFT+U method; b) the planar averaged electrostatic potential of the  $\text{Ag}_3\text{PO}_4@\text{NC}$  composite; c) 3D charge density difference ( $0.0005 \text{ e}/\text{bohr}^3$ ) for the  $\text{Ag}_3\text{PO}_4@\text{NC}$  composite (green and yellow areas indicate charge accumulation and depletion, respectively); the energy band charge density distributions ( $0.001 \text{ e}/\text{bohr}^3$ ) of d) the highest occupied energy band (HOEB) and e) the lowest unoccupied energy band (LUEB), the green and yellow colors represent the charge density distribution with and without electron occupation.

The charge density difference was obtained according to Equation (1).

$$\Delta\rho = \rho_{\text{Ag}_3\text{PO}_4(100)@\text{NC}} - \rho_{\text{Ag}_3\text{PO}_4(100)} - \rho_{\text{NC}} \quad (1)$$

where  $\rho_{\text{Ag}_3\text{PO}_4(100)@\text{NC}}$ ,  $\rho_{\text{Ag}_3\text{PO}_4(100)}$ , and  $\rho_{\text{NC}}$  are the charge densities of the composite,  $\text{Ag}_3\text{PO}_4(100)$ , and NC in the same configuration, respectively.<sup>[50,51]</sup> The charge accumulation was shown as the green region, and the charge depletion was shown as the yellow region. The change of charge density at the interfaces indicated that the electrons mainly transferred from NC to  $\text{Ag}_3\text{PO}_4$  through the interface. The net charge accumulation resulted in the formation of a built-in electric field at the  $\text{Ag}_3\text{PO}_4(100)@\text{NC}$  interface, and the electric field direction was from the NC surface to the  $\text{Ag}_3\text{PO}_4(100)$  surface, which was beneficial to the separation of photogenerated electrons and holes. In order to quantitatively explore the effective net charge transfer between the two constituents, charge analysis based on the Bader method were also performed, which indicated that there were 0.764 electron transfers from NC to  $\text{Ag}_3\text{PO}_4(100)$  (Table S3, Supporting Information).

The band charge density distribution of  $\text{Ag}_3\text{PO}_4@\text{NC}$  composite was calculated to further verify the migration of photogenerated carriers. As shown in Figure 5d,e, the highest occupied energy band (HOEB) of  $\text{Ag}_3\text{PO}_4@\text{NC}$  composite was occupied by the O and Ag orbitals that of  $\text{Ag}_3\text{PO}_4$ , whereas the lowest unoccupied energy band (LUEB) was occupied by the C and N orbitals that of NC. When the  $\text{Ag}_3\text{PO}_4(100)@\text{NC}$  composite exposed to the light, the photogenerated electrons at HOEB could easily excited to the LUEB, that is, the photogenerated electrons of  $\text{Ag}_3\text{PO}_4$  would be transferred to the NC surface and leaves behind the photogenerated holes at HOEB. Consequently, the photogenerated electrons would stay away from photogenerated holes, which effectively separated the photogenerated carriers and improved the catalytic performance of the composite photocatalyst.

In addition, the work function of the surface was also calculated to investigate the charge transfer of the interface, and the results are shown in Figure 6. The work functions of the

$\text{Ag}_3\text{PO}_4(100)$  and NC surfaces were calculated according to Equation (2).

$$\Phi = E_{\text{vac}} - E_F \quad (2)$$

where  $E_{\text{vac}}$  and  $E_F$  are electrostatic potential of vacuum energy and Fermi energy, respectively. The calculated work functions of the  $\text{Ag}_3\text{PO}_4(100)$  and monolayer NC were 5.64 and 3.29 eV, respectively. Because the Fermi energy of the  $\text{Ag}_3\text{PO}_4(100)$  surface was lower than that of the NC, when the  $\text{Ag}_3\text{PO}_4(100)$  surface contacted with NC, electrons will transfer from NC to the  $\text{Ag}_3\text{PO}_4(100)$ .<sup>[52–54]</sup> This leads to the decrease of the electronic density of NC and the increase of  $\text{Ag}_3\text{PO}_4(100)$ , implying the formation of built-in electric field at the interface of  $\text{Ag}_3\text{PO}_4(100)$  and NC, and the direction of the built-in electric field was from the NC surface to the  $\text{Ag}_3\text{PO}_4$  surface. These results were coincided well with the results of 3D charge density difference. When the  $\text{Ag}_3\text{PO}_4(100)@\text{NC}$  composite was excited by visible light, the photogenerated electrons of  $\text{Ag}_3\text{PO}_4$  would migrate to NC driven by the built-in electric field.

The above results indicated that the introduction of NC could form a built-in electric field at the interface of NC and  $\text{Ag}_3\text{PO}_4$ . In order to investigate the contribution of N element doping to the formation of built-in electric field, the model of undoped carbon and  $\text{Ag}_3\text{PO}_4@\text{carbon}$  were also constructed, and the charge transfer at interface was calculated by Bader method. The result in Table S3, Supporting Information, indicated that there was just 0.298 electron transfer from carbon slab to  $\text{Ag}_3\text{PO}_4(100)$ . Compared with the  $\text{Ag}_3\text{PO}_4(100)@\text{NC}$ , much less electron was transferred between the interface of undoped carbon and  $\text{Ag}_3\text{PO}_4(100)$ . Therefore, the doping of N was conducive to the formation of a larger built-in electric field at the interface.

In order to further reveal the role of N element in the formation of such a large electric field, the charge density and work function of NC and undoped carbon were calculated. As shown in Figure 7a,b, obviously, compared with the undoped carbon, NC possessed much higher charge density. It also could be found that the charge density around the N atom was the highest, and the charge density of all carbon atoms in NC

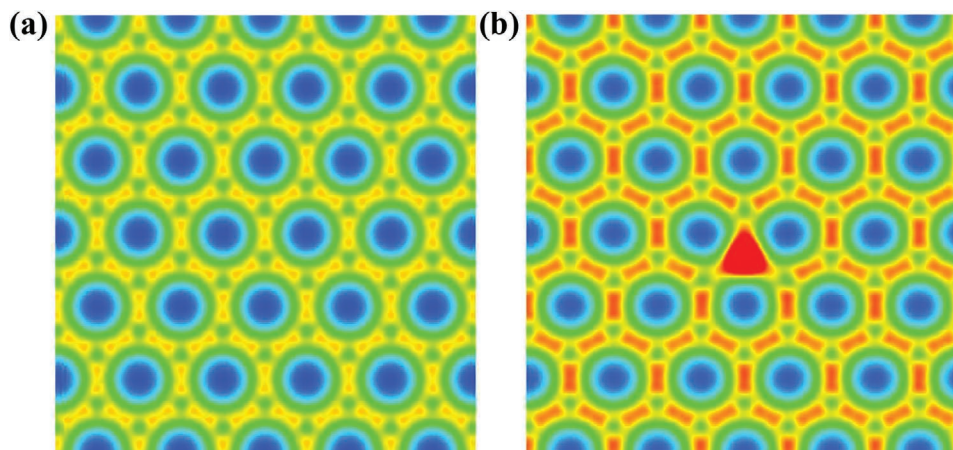


**Figure 6.** The charge density distribution for the undoped carbon a) and b) N-doped carbon. The range of the plot is from 0 to 2.6 e/Å<sup>3</sup>, and the plot has three sections: the lowest section ranging from 0 to 0.5 e/Å<sup>3</sup> is colored in blue, the section from 2.2 to 2.6 e/Å<sup>3</sup> shows the variation of the charge density in colors from blue to red, the highest section is all in red.

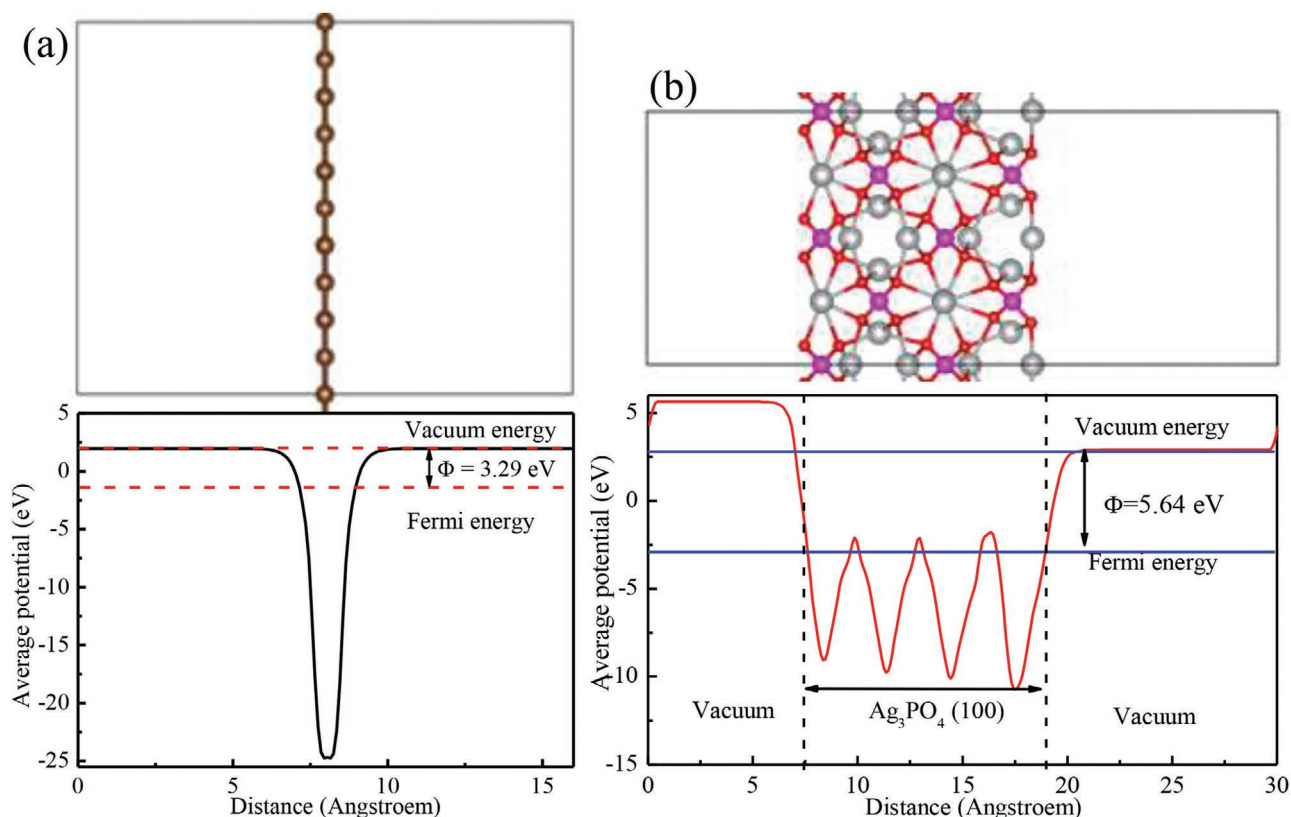


**Figure 7.** The profile of the planar average electrostatic potential and work functions for N-doped carbon a) and  $\text{Ag}_3\text{PO}_4(100)$  b).

was higher than that of undoped carbon atoms, indicating that the doping of N can increase the charge density of carbon. In addition, the work function of undoped carbon was calculated to be 4.45 eV, which was larger than that of NC (3.29 eV). Since their calculated vacuum energy was the same, the Fermi energy of undoped carbon was lower than that of NC, that is, the difference between the Fermi energy of undoped carbon and that of  $\text{Ag}_3\text{PO}_4$  was smaller (Figure S12, Supporting Information). This will result in a reduction of driving force between the interfaces. Therefore, due to the doping of N, a larger built-in electric field was formed at the interface of NC and  $\text{Ag}_3\text{PO}_4$ . The main reason was that the doping of N element made the carbon material have higher charge density and lower work function.

Based on the above experimental and calculated data, a possible mechanism for photocatalytic degradation of organic pollutants by the  $\text{Ag}_3\text{PO}_4@\text{NC}$  composite was proposed, as depicted in **Figure 8**. According to the above results, the CB and VB potential of  $\text{Ag}_3\text{PO}_4$  were calculated to be 0.44 eV, respectively. Therefore, under visible light irradiation, the  $\text{Ag}_3\text{PO}_4$  was easily excited through absorption of visible light, causing the formation of photogenerated electrons and holes. Because of the introduction of NC, a large built-in electric field was formed at the interface of NC and  $\text{Ag}_3\text{PO}_4$ , and the direction of the electric field was from the NC surface to the  $\text{Ag}_3\text{PO}_4$  surface. Driven by the electric field, the photogenerated electrons of  $\text{Ag}_3\text{PO}_4$  were rapidly transferred to the surface of NC, and then reacted with oxygen and water to form  $\cdot\text{O}_2^-$  and  $\cdot\text{OH}$ ,

which can attack and oxidize organic pollutants. The left behind photogenerated holes had a valence band potential of 2.78 eV, so it has strong oxidation ability, and can directly oxidize and decompose pollutants effectively. Meanwhile, under built-in electric field driving, the efficient separation of photogenerated electrons and holes prolonged their lifetime, increased the probability of photogenerated carriers participating in the redox reaction on the surface of catalysts, and effectively improved the photocatalytic performance of  $\text{Ag}_3\text{PO}_4@\text{NC}$  composite.

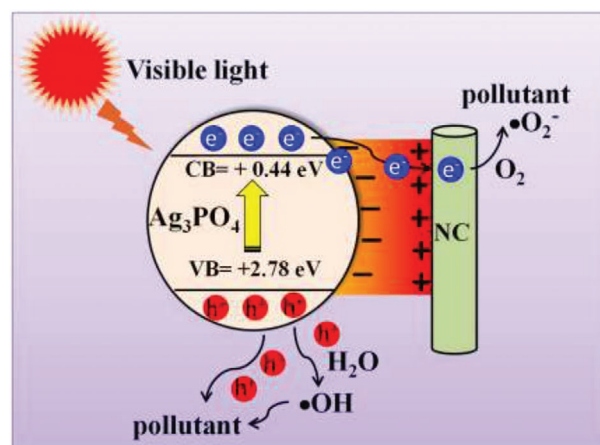


**Figure 8.** Schematic illustration of photocatalytic mechanism for  $\text{Ag}_3\text{PO}_4@\text{NC}$  composite under visible light irradiation.



### 3. Conclusions

In summary, N-doped carbon with hollow structure was successfully applied to prepare a novel photocatalyst  $\text{Ag}_3\text{PO}_4@\text{NC}$  which achieved excellent visible-light-driven catalytic performance and stability. The DFT calculation results, including the 3D charge density difference, band decomposed charge density, work function, and Bader charge analysis, indicated the successful construction of built-in electric field at the interface of catalyst composite. The photocatalyst exhibited superior catalytic activities on degradation of norfloxacin, diclofenac, and phenol, and reached 100% removal in 5, 8, and 12 min of visible light irradiation, respectively. The results of photodegradation experiments under sunlight irradiation demonstrated that the photocatalyst could effectively utilize natural sunlight for environmental treatment. The results of this study could be instructive for the design and development of highly efficient visible light response photocatalysts, and also provided a promising photocatalyst for the removal of recalcitrant organic pollutants.

### 4. Experimental Section

**Chemicals:** Diclofenac (DFC), norfloxacin (NFL), tris base, and dopamine hydrochloride were purchased from Sigma-Aldrich. Silver nitrate ( $\text{AgNO}_3$ ), ammonium chloride ( $\text{NH}_4\text{Cl}$ ), potassium permanganate ( $\text{KMnO}_4$ ), ethanol ( $\text{CH}_3\text{CH}_2\text{OH}$ ), disodium hydrogen phosphate dodecahydrate ( $\text{Na}_2\text{HPO}_4 \cdot 12\text{H}_2\text{O}$ ), phenol, and oxalic acid were obtained from Sinopharm Chemical Reagent Co. Ltd., China. All the chemicals were used without further purification. Deionized water was used in the whole experimental process.

#### Preparation of Samples

**Synthesis of  $\text{MnO}_2$ :** The  $\text{MnO}_2$  nanowires were synthesized according to a modified hydrothermal method.<sup>[31]</sup> First, 1 mmol  $\text{NH}_4\text{Cl}$  and 1 mmol  $\text{KMnO}_4$  were dissolved in the deionized water (30 mL), respectively. Then,  $\text{NH}_4\text{Cl}$  solution was poured into the  $\text{KMnO}_4$  solution and stirred for 10 min, and then the mixture was poured into the Teflon-lined stainless steel autoclave. The autoclave was heated up to 200 °C and held for 24 h. Finally, the product was recovered by centrifugation, washed by ethanol and deionized water, and dried overnight in vacuum (60 °C).

**Synthesis of  $\text{MnO}_2@\text{PDA}$ :** The prepared  $\text{MnO}_2$  nanowires were dispersed into a tris-buffer solution (10 mM, 200 mL) via sonication for 30 min. Then, 100 mg of dopamine hydrochloride was added to the above  $\text{MnO}_2$  suspension with magnetic stirring for 4 h. The obtained  $\text{MnO}_2@\text{PDA}$  product was washed with ethanol and deionized water several times, and dried in vacuum (60 °C).

**Synthesis of  $\text{MnO}_2@\text{NC}$  and N-Doped Carbon:** As-prepared  $\text{MnO}_2@\text{PDA}$  was annealed in  $\text{N}_2$  flow at 500 °C for 3 h with a heating rate of 1 °C min<sup>-1</sup>. The resultant  $\text{MnO}_2@\text{NC}$  product was then dispersed in oxalic acid (0.5 M, 40 mL) and stirred at 70 °C for 12 h to completely remove the  $\text{MnO}_2$  template. Finally, the produced N-doped carbon was collected by centrifugation, washed with ethanol and deionized water several times, and dried in vacuum (60 °C).

**Synthesis of  $\text{Ag}_3\text{PO}_4$  and  $\text{Ag}_3\text{PO}_4@\text{NC}$ :** The preparation of pure  $\text{Ag}_3\text{PO}_4$  and  $\text{Ag}_3\text{PO}_4@\text{NC}$  was generally based on the previously reported method, and the  $\text{Ag}_3\text{PO}_4@\text{NC}$  composite was synthesized by electrostatically driven self-assembly.<sup>[55]</sup> Briefly, 0.01 g NC was first dispersed in 400 mL deionized water, and the NC suspension was obtained after ultrasonic treatment for 1 h. Different volumes of NC dispersion were diluted to 100 mL. Then, 20 mL aqueous solution containing 1.53 g  $\text{AgNO}_3$  was added to the above NC suspension and stirred vigorously for 12 h. Afterward, added  $\text{Na}_2\text{HPO}_4 \cdot 12\text{H}_2\text{O}$  aqueous solution to the mixture at a dropping speed of 0.1 mL min<sup>-1</sup>, and kept stirring for 6 h. Finally, the obtained samples were washed by deionized water, and dried overnight in vacuum (60 °C). For comparison, pure

$\text{Ag}_3\text{PO}_4$  was also prepared under conditions identical to those of  $\text{Ag}_3\text{PO}_4@\text{NC}$  in the absence of NC.

### Supporting Information

Supporting Information is available from the Wiley Online Library or from the author.

### Acknowledgements

This work was supported by the National Natural Science Foundation of China (Grant Nos.: 51978178, 51478172, and 51521006), the Department of Science and Technology of Guangdong Province of China (Contract Nos.: 2019A1515012044 and 2018S0011), the International S&T Cooperation Program of China (Contract No.: 2015DFG92750), and the Department of Science and Technology of Hunan Province of China (Contract Nos.: 2017JJ2029 and 2017SK2362).

### Conflict of Interest

The authors declare no conflict of interest.

### Keywords

density functional theory, electric field, N-doped carbon, photocatalysis, silver phosphate

Received: April 1, 2020

Revised: May 25, 2020

Published online:

- [1] C. Liu, Y. Min, A. Y. Zhang, Y. Si, J. J. Chen, H. Q. Yu, *Water Res.* **2019**, *165*, 114980.
- [2] L. Zhao, D. L. Xiao, Y. Liu, H. C. Xu, H. Y. Nan, D. P. Li, Y. Kan, X. D. Cao, *Water Res.* **2020**, *172*, 115494.
- [3] M. F. Meyer, S. M. Powers, S. E. Hampton, *Environ. Sci. Technol.* **2019**, *53*, 12961.
- [4] D. Awfa, M. Ateia, M. Fujii, M. S. Johnson, C. Yoshimura, *Water Res.* **2018**, *142*, 26.
- [5] Q. Fu, D. Fedrizzi, V. Kosfeld, C. Schlechtriem, V. Ganz, S. Derrer, D. Rentsch, J. Hollender, *Environ. Sci. Technol.* **2020**, *54*, 4400.
- [6] B. Szymczycha, M. Borecka, A. Bialk-Bielinska, G. Siedlewicz, K. Pazdro, *Sci. Total Environ.* **2020**, *713*, 136522.
- [7] H. Li, J. Chen, H. J. Hou, H. Pan, X. X. Ma, J. K. Yang, L. L. Wang, J. C. Crittenden, *Water Res.* **2017**, *126*, 274.
- [8] Y. Hermans, A. Klein, H. P. Sarker, M. N. Huda, H. Junge, T. Toupance, W. Jaegermann, *Adv. Funct. Mater.* **2020**, *30*, 1910432.
- [9] H. Yamashita, K. Mori, Y. Kuwahara, T. Kamegawa, M. Wen, P. Verma, M. Che, *Chem. Soc. Rev.* **2018**, *47*, 8072.
- [10] X. D. Lv, X. T. Li, C. Yang, X. Q. Ding, Y. F. Zhang, Y. Z. Zheng, S. Q. Li, X. N. Sun, X. Tao, *Adv. Funct. Mater.* **2020**, *30*, 1910830.
- [11] D. J. Martin, G. Liu, S. J. Moniz, Y. Bi, A. M. Beale, J. H. Ye, J. W. Tang, *Chem. Soc. Rev.* **2015**, *44*, 7808.
- [12] A. Sharma, N. Liu, Q. Ma, H. Zheng, N. Kawazoe, G. Chen, Y. Yang, *Chem. Eng. J.* **2020**, *385*, 123765.
- [13] X. C. Yu, Y. Lin, H. Y. Liu, C. P. Yang, Y. R. Peng, C. Du, S. H. Wu, X. Li, Y. Y. Zhong, *J. Colloid Interface Sci.* **2020**, *561*, 379.



- [14] Y. Bi, S. Ouyang, N. Umezawa, J. Cao, J. H. Ye, *J. Am. Chem. Soc.* **2011**, 133, 6490.
- [15] C. T. Dinh, T. D. Nguyen, F. Kleitz, T. O. Do, *Chem. Commun.* **2011**, 47, 7797.
- [16] J. Zwara, E. Grabowska, T. Klimczuk, W. Lisowski, A. Zaleska-Medynska, *J. Photoch. Photobio. A: Chem.* **2018**, 367, 240.
- [17] D. J. Martin, N. Umezawa, X. Chen, J. H. Ye, J. W. Tang, *Energy Environ. Sci.* **2013**, 6, 3380.
- [18] M. Rehan, A. Barhoum, T. A. Khattab, L. Gätjen, R. Wilken, *Cellulose* **2019**, 26, 5437.
- [19] A. B. Trench, T. R. Machado, A. F. Gouveia, M. Assis, L. G. da Trindade, C. Santos, A. Perrin, C. Perrin, M. Oliva, J. Andrés, E. Longo, *Appl. Catal., B* **2018**, 238, 198.
- [20] V. G. Deonikar, P. V. Rathod, A. M. Pornea, H. Kim, *J. Environ. Manage.* **2020**, 256, 109930.
- [21] R. T. Chen, S. Pang, H. Y. An, J. Zhu, S. Ye, Y. Y. Gao, F. T. Fan, C. Li, *Nat. Energy* **2018**, 3, 655.
- [22] Y. Yu, W. Yan, X. F. Wang, P. Li, W. Gao, H. H. Zou, S. M. Wu, K. J. Ding, *Adv. Mater.* **2018**, 30, 1705060.
- [23] P. Cui, D. Wei, J. Ji, H. Huang, E. D. Jia, S. Y. Dou, T. Y. Wang, W. J. Wang, M. C. Li, *Nat. Energy* **2019**, 4, 150.
- [24] R. Matsuoka, R. Sakamoto, K. Hoshiko, S. Sasaki, H. Masunaga, K. Nagashio, H. Nishihara, *J. Am. Chem. Soc.* **2017**, 139, 3145.
- [25] L. W. Zhang, H. B. Fu, Y. F. Zhu, *Adv. Funct. Mater.* **2008**, 18, 2180.
- [26] S. B. Wang, B. Y. Guan, L. Yu, X. W. Lou, *Adv. Mater.* **2017**, 29, 1702724.
- [27] R. L. Liu, D. Q. Wu, X. L. Feng, K. Mullen, *Angew. Chem., Int. Ed.* **2010**, 49, 2565.
- [28] S. B. Wang, B. Y. Guan, X. Wang, X. W. Lou, *J. Am. Chem. Soc.* **2018**, 140, 15145.
- [29] L. Yu, H. Hu, H. B. Wu, X. W. Lou, *Adv. Mater.* **2017**, 29, 1604563.
- [30] X. F. Yang, H. Y. Cui, Y. Li, J. L. Qin, R. X. Zhang, H. Tang, *ACS Catal.* **2013**, 3, 363.
- [31] S. B. Wang, B. Y. Guan, X. W. Lou, *Energy Environ. Sci.* **2018**, 11, 306.
- [32] S. H. Wu, Y. Lin, C. P. Yang, C. Du, Q. Teng, Y. Ma, D. M. Zhang, L. J. Nie, Y. Y. Zhong, *Chemosphere* **2019**, 237, 124478.
- [33] L. Zhao, Y. S. Hu, H. Li, Z. X. Wang, L. Q. Chen, *Adv. Mater.* **2011**, 23, 1385.
- [34] S. H. Wu, H. Y. Liu, C. P. Yang, X. Li, Y. Lin, K. Yin, J. T. Sun, Q. Teng, C. Du, Y. Y. Zhong, *Chem. Eng. J.* **2020**, 392, 123683.
- [35] L. Liu, L. Ding, Y. G. Liu, W. J. An, S. D. Lin, Y. H. Liang, W. Q. Cui, *Appl. Catal., B* **2017**, 201, 92.
- [36] Z. J. Sun, H. F. Zheng, J. S. Li, P. W. Du, *Energy Environ. Sci.* **2015**, 8, 2668.
- [37] Y. Zhou, X. J. Zhang, Q. Zhang, F. Dong, F. Wang, Z. Xiong, *J. Mater. Chem. A* **2014**, 2, 16623.
- [38] C. Y. Feng, Y. C. Deng, L. Tang, G. M. Zeng, J. J. Wang, J. J. Yu, Y. N. Liu, B. Peng, H. P. Feng, J. J. Wang, *Appl. Catal., B* **2018**, 239, 525.
- [39] H. Y. Zhu, R. Jiang, J. B. Li, Y. Q. Fu, S. T. Jiang, J. Yao, *Sep. Purif. Technol.* **2017**, 179, 184.
- [40] J. L. Wang, S. Z. Wang, *Chem. Eng. J.* **2018**, 334, 1502.
- [41] C. P. Yang, H. Qian, X. Li, Y. Cheng, H. J. He, G. M. Zeng, J. Y. Xi, *Trends Biotechnol.* **2018**, 36, 673.
- [42] H. M. Hegab, A. ElMekawy, B. van den Akker, M. Ginic-Markovic, C. Saint, G. Newcombe, D. Pant, *Rev. Environ. Sci. Biotechnol.* **2018**, 17, 147.
- [43] A. Fernandez-Naveira, H. N. Abubackar, M. C. Veiga, C. Kennes, *World J. Microbiol. Biotechnol.* **2017**, 33, 43.
- [44] Y. Lin, S. H. Wu, X. Li, X. Wu, C. P. Yang, G. M. Zeng, Y. R. Peng, Q. Zhou, L. Lu, *Appl. Catal., B* **2018**, 227, 557.
- [45] Y. Lin, S. H. Wu, C. P. Yang, M. Chen, X. Li, *Appl. Catal., B* **2019**, 245, 71.
- [46] J. Cao, S. W. Sun, X. Li, Z. H. Yang, W. P. Xiong, Y. Wu, M. Y. Jia, Y. Y. Zhou, C. Y. Zhou, Y. Zhang, *Chem. Eng. J.* **2020**, 382, 122802.
- [47] L. J. Xu, J. L. Wang, *Environ. Sci. Technol.* **2012**, 46, 10145.
- [48] X. P. Huang, Y. Chen, E. Walter, M. R. Zong, Y. Wang, X. Zhang, O. Qafoku, Z. M. Wang, K. M. Rosso, *Environ. Sci. Technol.* **2019**, 53, 10197.
- [49] S. H. Wu, H. Y. Liu, Y. Lin, C. P. Yang, W. Lou, J. T. Sun, C. Du, D. M. Zhang, L. J. Nie, K. Yin, Y. Y. Zhong, *Chemosphere* **2020**, 244, 125490.
- [50] Y. Si, H. Y. Wu, H. M. Yang, W. Q. Huang, K. Yang, P. Peng, G. F. Huang, *Nanoscale Res. Lett.* **2016**, 11, 495.
- [51] Y. Lin, H. Y. Liu, C. P. Yang, X. Wu, C. Du, L. M. Jiang, Y. Y. Zhong, *Appl. Catal., B* **2020**, 264, 118479.
- [52] J. J. Liu, B. Cheng, J. G. Yu, *Phys. Chem. Chem. Phys.* **2016**, 18, 31175.
- [53] G. Singh-Bhalla, C. Bell, J. Ravichandran, W. Siemons, Y. Hikita, S. Salahuddin, A. F. Hebard, H. Y. Hwang, R. Ramesh, *Nat. Phys.* **2011**, 7, 80.
- [54] X. M. Ning, Y. L. Wu, X. F. Ma, Z. Zhang, R. Q. Gao, J. Chen, D. L. Shan, X. Q. Lu, *Adv. Funct. Mater.* **2019**, 29, 1902992.
- [55] Y. Lin, X. Wu, Y. Han, C. P. Yang, Y. Ma, C. Du, Q. Teng, H. Y. Liu, Y. Y. Zhong, *Appl. Catal., B* **2019**, 258, 117969.